Physical properties of the quasi-two-dimensional square lattice antiferromagnet math xmlns="http://www.w3.org/1998/Math/MathML">mrow>msub>mi>Ba/mi>mn>2/mn>/msub>msub>mi>FeSi/mi>mn>2/mn>/msub>msub>mi mathvariant="normal">O/mi>mn>7/mn>/msub>/mrow>/math>

Tae-Hwan Jang, Seung-Hwan Do, Minseong Lee, Hui Wu, Craig M. Brown, Andrew D. Christianson, Sang-Wook Cheong, and Jae-Hoon Park

Physical properties of a quasi-two-dimensional square lattice antiferromagnet Ba₂FeSi₂O₇

Tae-Hwan Jang,[1] Seung-Hwan Do,[1,2] Minseong Lee,[3] Hui Wu,[4] Craig M. Brown,[4] Andrew D. Christianson,[2] Sang-Wook Cheong,[1, 5, 6] and Jae-Hoon Park[1, 7*]

[1]*MPPHC-CPM, Max Planck POSTECH/Korea Research Initiative, Pohang 37673, Republic of Korea*

[2]*Materials Science and Technology Division, Oak Ridge National Laboratory, Oak Ridge, Tennessee 37831, USA*

[3]*National High Magnetic Field Laboratory (NHMFL), Los Alamos National Laboratory (LANL), Los Alamos, New Mexico 87545, USA*

[4]*NIST Center for Neutron Research, National Institute of Standards and Technology, Gaithersburg, Maryland 20899, USA*

[5]*l_PEM, Department of Physics, Pohang University of Science and Technology, Pohang 37673, Republic of Korea*

[6]*Ruters Center for Emergent Materials and Department of Physics and Astronomy, Rutgers University, Piscataway, New Jersey 08854, USA*

[7]*Department of Physics, Pohang University of Science and Technology, Pohang 37673, Republic of Korea*

ABSTRACT

We report magnetization (χ, M), magnetic specific heat (C_M), and neutron powder diffraction results on a quasi-two-dimensional (2D) $S = 2$ square lattice antiferromagnet $Ba_2FeSi_2O_7$ consisting of FeO_4 tetrahedrons with highly compressive tetragonal distortion (27%). Despite of the quasi-2D lattice structure, both χ and C_M present three dimensional magnetic long-range ordering below the Néel temperature $T_N = 5.2$ K. Neutron diffraction data shows a collinear $\boldsymbol{Q_m} = (1,0,1/2)$ antiferromagnetic (AFM) structure below T_N but the ordered moment aligned in the ab plane is suppressed by 26% from the ionic spin $S = 2$ value ($4\mu_B$) . Both the AFM structure and the suppressed moments are well explained by using Monte Carlo simulations with a large single-ion in-plane anisotropy $D = 1.4$ meV and a rather small Heisenberg exchange $J_{intra} = 0.15$ meV in the plane. The characteristic 2D spin fluctuations are recognized in the magnetic entropy release and diffuse scattering above T_N. This new quasi-2D magnetic system also displays unusual non-monotonic dependence of T_N as a function of magnetic field H.

I. INTRODUCTION

Two-dimensional (2D) Heisenberg antiferromagnets have been intensively studied both in theory and in experiment to explore exotic low-dimensional magnetic behaviors. The Mermin-Wagner theorem states that no long range magnetic order can be stabilized at finite temperature in the 2D Heisenberg magnetic system due to strong spin fluctuations [1]. However, lattice topology and strong magnetic anisotropy are predicted to be able to realize the 2D AFM ground state [2] as in 2D-Ising and 2D-XY spin systems under an external magnetic field [3-7]. In real layered magnetic materials [8-10], three-dimensional long-range magnetic ordering has often been observed because of the quasi-2D nature with minimal but non-vanishing interlayer magnetic coupling [11, 12].

Melilite compounds $A_2MB_2O_7$ (A = Ca, Sr, Ba, M = divalent $3d$ transition metals, B = Si, Ge) are interesting examples of quasi-2D square lattice Heisenberg AFM systems. The d-p metal-ligand

hybridization have been reported to induce various interesting physics such as distinct magnetoelectricity [13], directional dichroism involving spin wave/optical excitations [14], magnetochiral effects [15], and longitudinal magnon modes associated with electromagnons [16, 17]. Most studies have been performed on melilite compounds with half-integer spin quantum numbers, M = Mn (5/2), Co (3/2), Cu(1/2) in the last decades. Meanwhile, the studies on the compounds with an integer spin number such as M = Ni^{2+} (S = 1) or Fe^{2+} (S = 2) have rarely been carried out due to lack of crystals with reliable quality, and thus only a few ones have been reported recently: a theoretical work on Jahn-Teller distortion driven ferroelectricity in Ba$_2$NiGe$_2$O$_7$ [18] and a THz experimental one on spin-orbital excitations in Sr$_2$FeSi$_2$O$_7$ [19]. Especially, the Fe (S = 2) based compounds present strongly compressed FeO$_4$ tetrahedrons along the c axis suggesting intriguing magnetic properties governed by a non-trivial magnetic gap [19-22].

A melilite compound Ba$_2$FeSi$_2$O$_7$ is crystallized in the $P\bar{4}2_1m$ tetragonal melilite structure as shown in Fig. 1(a) [23]. The lattice constants are a = 8.3261 Å and c = 5.3401 Å at room temperature. The system is composed of FeO$_4$ tetrahedra connected via SiO$_4$ polyhedra, and FeSi$_2$O$_7$ layers are separated by Ba layers to form a quasi 2D square-lattice structure. The magnetic coupling is dominated by the intra-layer Heisenberg interaction (J_{intra}) through the neighboring Fe^{2+}-O^{2-}-O^{2-}-Fe^{2+} exchange path and the layered structure contributes a minimal inter-plane exchange interaction (J_{inter}), resulting in a quasi-2D magnetic system. Noticeably, the FeO$_4$ tetrahedron is compressed by as large as 27% along the c axis with respect to the perfect tetrahedron. Such a large compression splits both the triplet t$_{2g}$ and doublet e$_g$ orbital states and produce a considerable unquenched orbital angular momentum, which is responsible for noticeable single-ion anisotropy (D) [20, 21]. Considering that D ~ 1.1 meV was estimated in Ba$_2$CoGe$_2$O$_7$ of 13% compressed CoO$_4$ tetrahedrons [16, 24, 25], the D value is certainly enhanced in Ba$_2$FeSi$_2$O$_7$ with 27% compression of the FeO$_4$ tetrahedron.

In this article, we investigate physical properties of this quasi-2D integer spin (S = 2) AFM Ba$_2$FeSi$_2$O$_7$ using magnetization, specific heat, and neutron powder diffraction measurements. The resu-
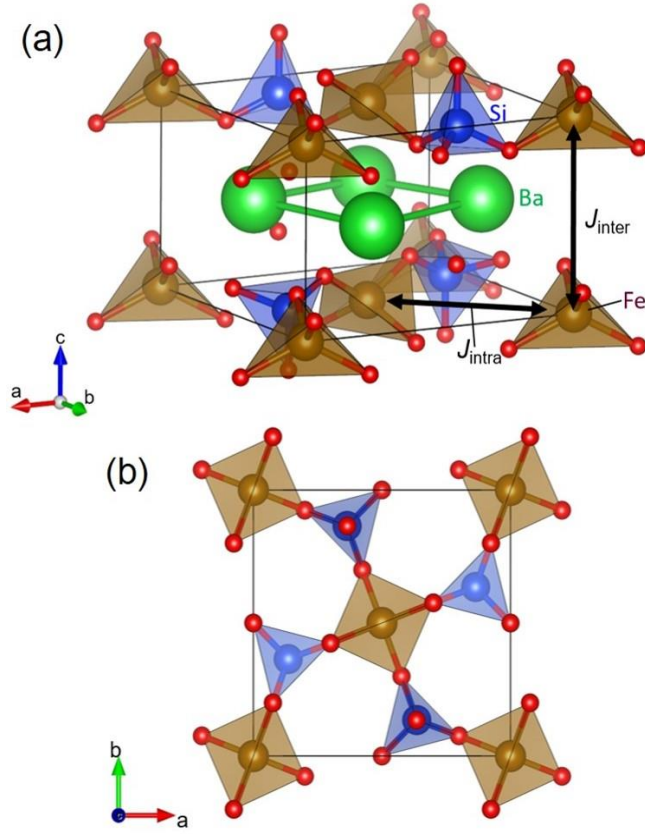
FIG. 1. (a) Crystal structure of $Ba_2FeSi_2O_7$ determined from the neutron diffractions. Thick black arrows indicate the in-plane (J_{intra}) and inter-plane (J_{inter}) nearest neighbor Heisenberg exchange interactions. (b) A single layer $FeSi_2O_7$ structure. J_{inter} is the exchange interaction between neighboring two Fe^{2+} spins through the Fe^{2+}-O^{2-}-O^{2-}-Fe^{2+} path.

lts manifest the AFM ordering below the Néel temperature ($T_N = 5.2$ K) with large easy-planar magnetic anisotropy. Using Monte Carlo simulations, we estimate $J_{intra}/D \sim 0.1$. The specific heat measurements reveal a Schottky anomaly arising from thermal populations on low-lying excited spin-orbital states. Neutron diffraction measurements reveal that short-range spin correlations appear below 20 K and that the AFM structure is characterized by a staggered magnetic moment of 2.95 μ_B, which is considerably (26%) smaller than the moment (4 μ_B) expected from $S = 2$. The field dependent measurements exhibit unusual non-monotonic behavior of $T_N(H)$ as a function of the H-field, indicating that the quasi-2D square lattice magnet $Ba_2FeSi_2O_7$ is a novel easy-planar integer spin system.

II. METHODS

To obtain single crystals of $Ba_2FeSi_2O_7$, we prepared a polycrystalline of $Ba_2FeSi_2O_7$ as a precursor using the solid-state reaction. Stoichiometric mixtures of $BaCO_3$, Fe_2O_3, and SiO_2 were thoroughly ground, pelletized, and heated at 1050°C with intermediate sintering. X-ray and neutron powder diffraction measurements on the polycrystalline samples identified a dominant phase of $Ba_2FeSi_2O_7$ (96.5%) with minor Ba_2SiO_4 (2.6%) and SiO_2 (0.9%) (see Fig. 6). The polycrystalline samples were prepared as feed rods, and a single crystal of $Ba_2FeSi_2O_7$ was grown using a floating zone melting method under reducing gas atmosphere. The growth direction was perpendicular to the c axis and the size of the as-grown crystal was about 8 mm in diameter and 60 mm in length. The powder XRD pattern on crushed crystals presents a single phase of $Ba_2FeSi_2O_7$, as described in Appendix A.

Temperature (T) and magnetic field (H) dependence of dc magnetization and specific heat measurements on a $Ba_2FeSi_2O_7$ crystal were performed by using a vibrating sample magnetometry (VSM) option and a standard calorimetric relaxation technique equipped in a physical property measurement system (PPMS) of Quantum Design DynaCool-9 T. The magnetization results were compared with classical Monte Carlo simulations in order to estimate the energy scale of the exchange interactions in $Ba_2FeSi_2O_7$. In the simulation, a square lattice of $16 \times 16 \times 6$ spin sites was employed with periodic boundary conditions.

Neutron powder diffraction measurements were carried out using the BT-1 High-Resolution Powder Diffractometer (HRPD) at NIST Center for Neutron Research (NCNR), USA. A 2.9 g of polycrystalline sample was loaded into a vanadium can and cooled with a flow-type cryostat. A constant wavelength λ = 2.0772 Å of the neutron beam was collimated by using a Ge (311)-60° monochromator. Diffraction data were collected at temperatures, 1.7, 3, 8, 10, 20, and 30 K. The data refinement was carried out in the Rietveld methods by using the FULLPROF program [26], and the software SARAh was used for representational analysis to determine symmetry-allowed magnetic structures [27].

5

III. EXPERIMENTAL RESULTS

A. Magnetic properties

Figure 2(a) shows temperature dependence of the magnetic susceptibility ($\chi = M/H$) for a Ba$_2$FeSi$_2$O$_7$ single crystal with magnetic fields parallel ($H\|ab\|[110]$) and perpendicular ($H\|c\|[001]$) to the ab plane. The magnetic susceptibility exhibits strongly anisotropic easy-planar spin behaviors over a broad temperature range. The ab plane is the magnetic easy plane and the c axis is the hard axis. At low temperatures, $\chi(T)$ for both field directions exhibit peaks around $T \sim 8$ K, corresponding to the onset of short-range magnetic order with 2D spin fluctuations. The AFM long-range ordering temperature is determined to be $T_N = 5.2$ K from the sharp peak in the first derivative of the in-plane magnetic susceptibility ($d\chi/dT$).

Inverses of the magnetic susceptibilities in Fig. 2(b) exhibit linear behaviors above 100 K, following the Curie-Weiss formula, $\chi(T) = \chi_0 + C/(T - \Theta_{CW})$ with the Curie constant C, the Curie-Weiss temperature Θ_{CW}, and the diamagnetic contribution χ_0. We determined an effective magnetic moment $\mu_{eff}[ab] = 5.56(1)\ \mu_B$, $\mu_{eff}[c] = 4.84(1)\ \mu_B$ and Curie-Weiss temperatures $\Theta_{CW}[ab] = -7.4(2)$ K, $\Theta_{CW}[c] = -23.7(2)$ K from Curie-Weiss fits in the temperature range from 100 K to 300 K. The out-of-plane moment $\mu_{eff}[c]$ is comparable to the spin only value of $S = 2$ ($\mu_{eff} \sim 4.9\ \mu_B$ for $g = 2$) while the in-plane one $\mu_{eff}[ab]$ is considerably larger than the value. It implies that an unquenched angular momentum is present and makes anisotropic contribution to the magnetic moment [21], in consistent with the observed anisotropic behavior of χ even up to room temperature. The obtained large $\Theta_{CW}[c]$ is attributed to the spin fluctuation involving spin-spin interaction with a strong 2D character.

Figure 3(a) presents isothermal magnetization $M(H)$ as a function of magnetic field H up to 9 T for $H\|ab\|[110]$ and $H\|c\|[001]$ at $T = 1.8$ K. $M(H)$ shows large anisotropy for $H\|ab$ and $H\|c$ reflecting the strong easy-planar spin, but both $M_{ab}(H) \equiv M(H\|ab)$ and $M_c(H) \equiv M(H\|c)$ show linear-like behaviors with H. Interestingly, the slope in $M_{ab}(H)$ changes considerably around $\mu_0H \sim 0.3$ T (μ_0H_{ab1})
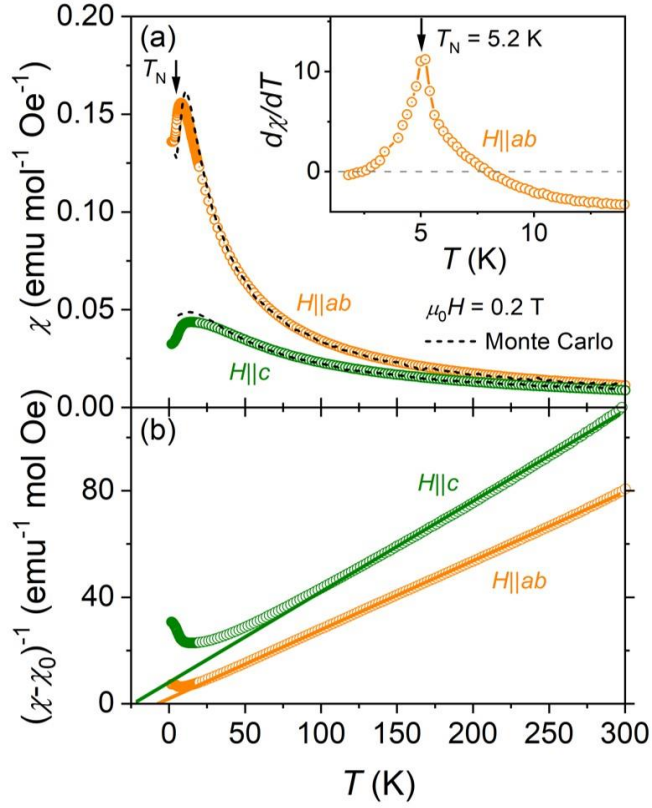
6

and ~

FIG. 2. (a) Temperature (T) dependence of the dc magnetic susceptibility ($\chi = M/H$) with applied magnetic fields $\mu_0 H = 0.2$ T along $H\|ab\|[110]$ (orange symbol) and $H\|c\|[001]$ (olive symbol). The dashed lines are the results of classical Monte Carlo simulations with $J_{intra} = 0.15$ meV, $J_{inter} = 0.0025$ meV, $D = 1.4$ meV with a field of 0.2 T. The first derivative of the magnetic susceptibility ($d\chi/dT$) is presented as a function of temperature in the inset. Vertical arrows in (a) denote the magnetic transition at $T_N = 5.2$ K. (b) Inverses of the magnetic susceptibilities with magnetic field along $H\|ab\|[110]$ (orange symbol) and $H\|c\|[001]$ (olive symbol). Solid lines are Curie-Weiss fits to the data from 100 K to 300 K.

7.4 T ($\mu_0 H_{ab2}$). As shown in Fig. 3(b), these anomalies are more noticeable in the derivative dM_{ab}/dH while those disappear at 6.5 K (> T_N), indicating that there exist two field-induced transitions below T_N. Meanwhile, M_c monotonically increases with H-field up to 9 T without any noticeable anomaly representing the field-induced transition. We also observed the weak anomaly around $\mu_0 H_{a1} \sim 0.5$ T in the dM/dH for $H\|a\|[100]$ at $T = 1.8$ K (Fig. 3(b)). As the magnetic field is applied away from the

7

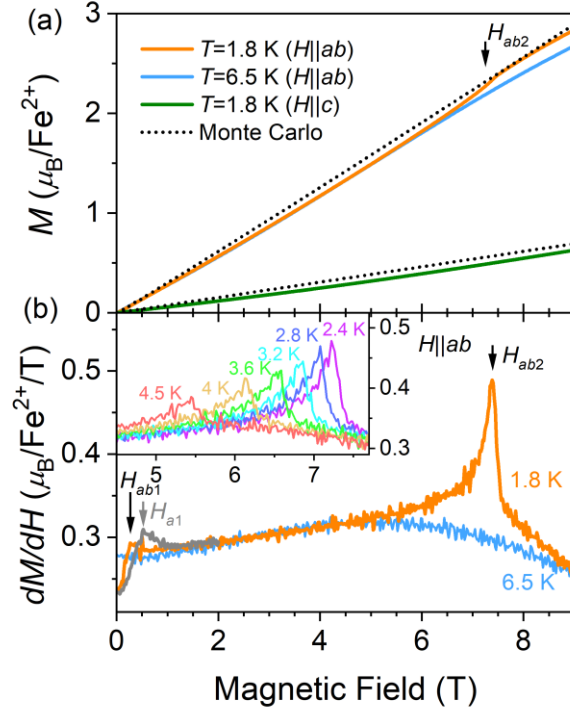easy axes, the Zeeman energy cost is required to increase the critical field for the transition. Thus,

FIG. 3. (a) Magnetic field (H) dependence of magnetization (M) curve along $H\|ab\|[110]$ (orange and blue symbols for $T = 1.8$ K and 6.5 K, respectively) and $H\|c\|[001]$ (olive symbol, $T = 1.8$ K). The dotted lines are the results of classical Monte Carlo simulations with $J_{intra} = 0.15$ meV, $J_{inter} = 0.0025$ meV and $D = 1.4$ meV (for detailed information about calculation, see the section IV.). (b) First derivative of magnetization curve (dM/dH) as a function of $H\|ab\|[110]$ at 1.8 K (orange symbol) and 6.5 K (blue symbol) and of $H\|a\|[100]$ at 1.8 K (grey symbol, up to 2 T). Vertical arrows indicate positions of critical magnetic fields $\mu_0 H_{ab1} \sim 0.3$ T ($\mu_0 H_{a1} \sim 0.5$ T) and $\mu_0 H_{ab2} \sim 7.4$ T showing the H induced weak and sharp peaks in dM/dH at $T = 1.8$ K, respectively. The inset in (b) displays dM/dH as a function of $H\|ab\|[110]$ measured at various temperatures below T_N.

slightly smaller value of $\mu_0 H_{ab1}$ than one of $\mu_0 H_{a1}$ implies that the easy axes are likely along [110] and [1-10] directions in the ab plane. We note that the dM/dH for both $H\|a\|[100]$ and $H\|b\|[010]$ shows almost the same H dependence and the critical magnetic fields (not shown here), indicating that the fourfold in-plane anisotropy exists by the crystallographic symmetry. The calculated in-plane magnetic anisotropy energy is about 0.05 meV.
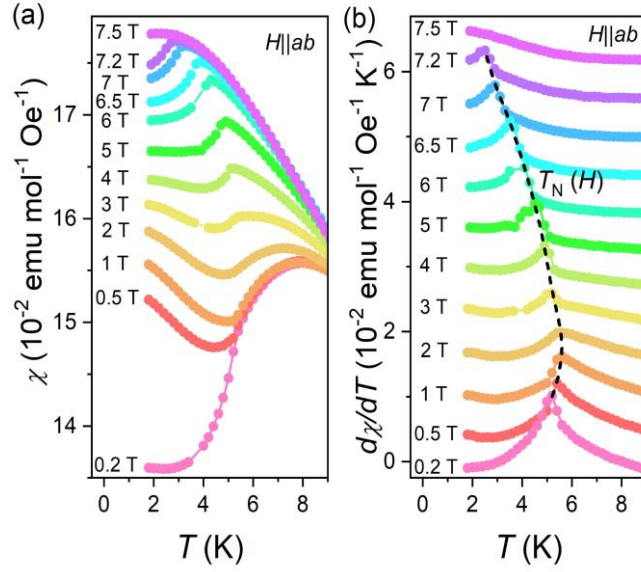
FIG. 4. (a) Temperature (T) dependence of the dc magnetic susceptibility ($\chi = M/H$) and (b) first derivatives of magnetic susceptibility ($d\chi/dT$) as a function of T for applied magnetic fields along $H\|ab\|[110]$. In (b), the dotted guide line indicates $T_N(H)$ determined from the peak positions in $d\chi/dT$. For clarity, each $d\chi/dT$ curve is vertically shifted by 0.006 emu mol^{-1} Oe^{-1} K^{-1}.

The low field transition at H_{ab1} can be attributed to a spin-flop-like transition aligning two AFM domains. At $H = 0$ field (AFM-I phase), there exist two equally-populated AFM domains: the AFM ordered spins along in-plane easy axis [110] in one and [1-10] in the other. At H increases across H_{ab1}, the spin axes of both domains align to be perpendicular to the H-direction in the ab plane (AFM-II phase). A similar transition was also observed in Ba$_2$CoGe$_2$O$_7$ [25]. H_{ab1} exhibits almost no temperature dependence below T_N (not shown here) and disappears above T_N. On the other hand, the high field transition enhances M_{ab} across H_{ab2}, and the enhanced magnetic moment $\Delta M_{ab}(T) = M_{ab}(T) - M_{ab}(6.5$ K$)$ is estimated to be ~ 0.15 μ_B/Fe^{2+} at $T = 1.8$ K. To trace the anomalies, we measured $M_{ab}(H)$ at different temperatures below T_N. The inset shows dM_{ab}/dH as a function of H at various temperatures below T_N. As temperature increases, the dM/dH peak feature becomes weaker and H_{ab2} shifts to low fields. The peak disappears above T_N, indicating that this transition is also relevant to the AFM order.

Figures 4(a) shows $\chi(T)$ as a function of temperature T measured at various $H\|ab\|[110]$ fields up to

$\mu_0 H = 7.5$ T. $\chi(T)$ below T_N suddenly changes between 0.2 T and 0.5 T due to the spin-flop-like transition across $\mu_0 H_{ab1} \sim 0.3$ T observed M_{ab} (dM_{ab}/dH). As presented in Fig. 4(b), the derivatives $d\chi/dT$ clearly exhibit peak features representing the AFM transition up to $\mu_0 H = 7.2$ T ($< \mu_0 H_{ab2}$) and enable us to determine $T_N(H)$ at a given $H\|ab$ field. Interestingly, $T_N(H)$ shows a non-monotonic field dependent behavior. $T_N(H)$ slightly increases as H increases up to $\mu_0 H \sim 2$ T, and then it decreases for further increasing H up to 7.2 T. At $\mu_0 H = 7.5$ T ($> \mu_0 H_{ab2}$), the $d\chi/dT$ peak feature becomes completely suppressed with saturation in $\chi(T)$.

B. Specific heat

Figure 5(a) shows total specific heat (C_P) of $Ba_2FeSi_2O_7$ at $H = 0$. Lattice contribution (C_L) was estimated from the Debye-Einstein model, where $C_L(T)$ is defined as [28, 29],

$$C_L(T) = m\left[9Rx_D^{-3}\int_0^{x_D}\frac{x^4 e^x}{(e^x - 1)^2}\right] + \sum_{i=1}^{s-1} n_i\left[3R\frac{x_{Ei}^2 e^{x_{Ei}}}{(e^{x_{Ei}} - 1)^2}\right]. \tag{1}$$

The first term represents the Debye specific heat for the acoustic phonon modes and the second term does the Einstein specific heat for optical phonon modes. x_D and x_{Ei} are defined as $x_D = \Theta_D/T$ and $x_{Ei} = \Theta_{Ei}/T$ where Θ_D and Θ_{Ei} are the Debye temperature and the Einstein temperatures, respectively. The constants m and n_i are the number of degrees of freedom for each contribution and R is the molar gas constant. Fitting Eq. (1) to the experimental data in a range from 70 K to 250 K provides $\Theta_D \sim 237$ K ($m = 4.8$), $\Theta_{E1} \sim 554$ K ($n_1 = 4.3$) and $\Theta_{E2} \sim 1345$ K ($n_2 = 2.9$) with $m + n_1 + n_2 = 12$ (total number of atoms in the formula unit). Based on these fitting parameters, the extracted C_L is displayed in Fig. 5(a). Magnetic specific heat (C_M) shown in Fig. 5(b) was obtained by subtracting the lattice contribution from the total specific heat, i.e. $C_M = C_P - C_L$. C_M displays a sharp λ-anomaly at $T_N = 5.2$ K, which coincides with T_N determined from the magnetic susceptibility. Above T_N, C_M exhibits a broad peak around $T_{SO} \sim 8$ K, which represents the short-range ordering with suppression of the long-range order due to the
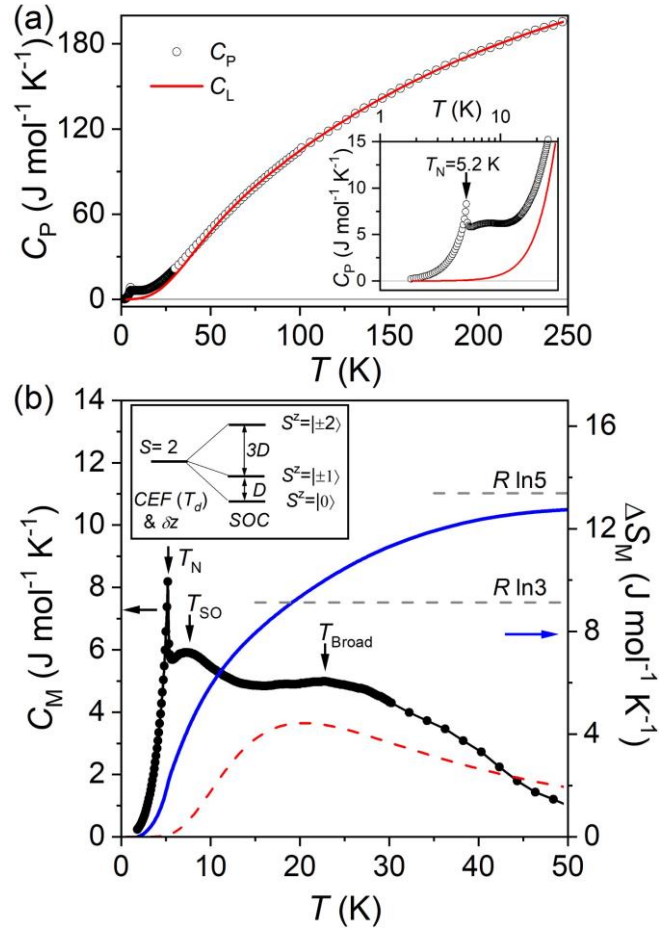
10

FIG. 5. (a) Total specific heat (C_P). Open circles and a red line display the measured total specific heat (C_P) and the calculated lattice contribution of specific heat (C_L), respectively. Inset displays the magnified C_P and C_L below 30 K in a semi-logarithmic scale. The vertical arrow indicates the magnetic transition temperature ($T_N = 5.2$ K). (b) Magnetic specific heat (left panel: $C_M = C_P - C_L$, black symbols) and magnetic entropy gain (right panel: ΔS_M, blue line) as a function of temperature. Above T_N, C_M shows two broad peaks centered at $T_{SO} \sim 8$ K and T_{Broad} ~ 23 K, associated with short-range spin correlations and a Schottky anomaly from the excitations between the spin S^z states, respectively. Two gray horizontal dashed lines show $R\ln(2S+1)$ for $S = 1$ ($R\ln3$) and $S = 2$ ($R\ln5$). Inset represents the energy level structure of the lowest d_{z^2} orbital for the Fe^{2+} ion in the tetrahedral crystal field (T_d) with a tetragonal compression (δz) and energy levels of the S^z states further split by the spin-orbit coupling (SOC) [19, 20]. A red dashed curve indicates the calculated Schottky anomaly for the transition between $S^z = |\pm 2\rangle$ and $S^z = |\pm 1\rangle$ states with gap, $\Delta = 3D = 3*1.4$ meV $= 4.2$ meV where D is referred to the Monte Carlo calculations (see the text).

low-dimensionality [2].

The magnetic entropy, $\Delta S_M(T)$, was calculated by using $\Delta S_M(T) = \int_0^T \Delta C_M(T)/T \, dT$. ΔS_M at $T =$ 50 K is obtained to be 12.74 J mol^{-1} K^{-1} that corresponds to 95% of $R\ln(2S+1) = R\ln5$, the total entropy of $S = 2$. We note that only about 20% of the total entropy is released at T_N and additional entropy involving the short range order is released by above the transition temperature ($T_{SO} \sim 8$ K). Interestingly, the entropy $R\ln(3) \sim 9.13$ J mol^{-1} K^{-1} corresponding to the degree of freedom for $S = 1$ effectively releases up to around 18 K, where the short-range ordering peak diminishes. Above this temperature, a Schottky-like broad peak is visible in C_M around $T_{Broad} \sim 23$ K and the entropy gradually releases the remnant of the $S = 2$ spin degree of freedom upto even above 50 K.

C. Powder neutron diffraction

To study the AFM spin structure below T_N, we have carried out zero field ($H = 0$) neutron powder diffraction (NPD) measurements on Ba$_2$FeSi$_2$O$_7$. Figure 6 shows the NPD patterns at 30 K ($> T_N$) and 1.7 K ($< T_N$). The crystal and magnetic structures were determined from the Rietveld refinement fitting by using FULLPROF [26]. The refined crystallographic parameters are tabulated in Table I ($T = 30$ K) and II ($T = 1.7$ K). Both the $T = 30$ K and $T = 1.7$ K diffraction patterns for the nuclear Bragg peaks are well described by the tetragonal space group, $P\overline{4}2_1m$ (SG: 113), and the Bragg peak profiles exhibit only small variations across T_N, evidencing that the AFM transition does not accompany any considerable structural transition. Comparing the low Q-region (0.5 Å$^{-1} \leq Q \leq 2.0$ Å^{-1}) diffraction patterns at $T = 1.7$ K and 30 K as shown in the inset, we identify the magnetic Bragg reflections at $\boldsymbol{Q} =$ (1,0,1/2) and (2,1,1/2) below T_N, indicating the characteristic vector of $\boldsymbol{Q_m} = $ (1,0,1/2).

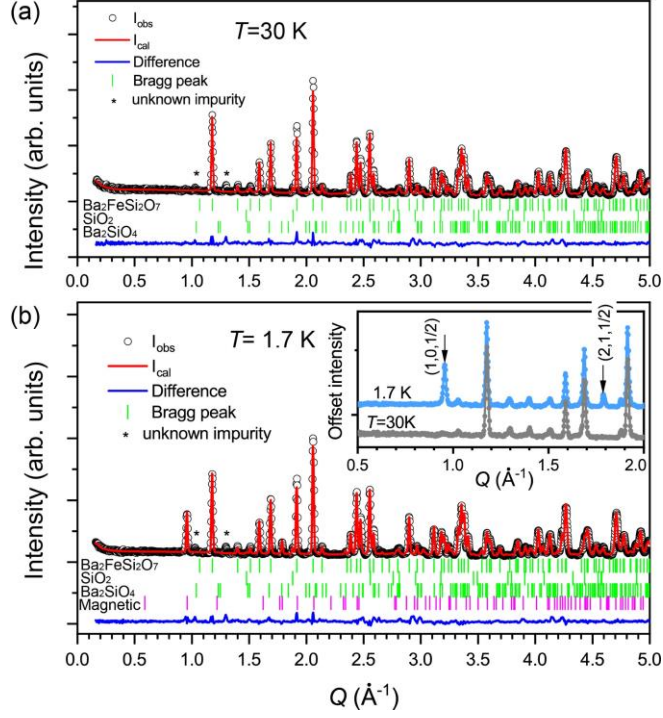Representation analyses were used to determine symmetry-allowed magnetic structures. Irreducible

FIG. 6. Neutron powder diffraction patterns for $Ba_2FeSi_2O_7$ at (a) $T = 30$ K ($> T_N$) and (b) 1.7 K ($< T_N$). Open circles and a red solid line represent the experimental data and the Rietveld refinement fitting line, respectively. At both temperatures, Bragg peaks from SiO_2 and Ba_2SiO_4 (non-magnetic secondary phases) are visible in the sample, and the Rietveld refinement quantifies the phase fractions of 0.9% and 2.6%, respectively. In (b), the structural and magnetic Bragg reflections are presented by upper (green) and low (violet) ticks, respectively. The inset shows an expanded view of the low-Q region data and miller indexed magnetic peaks indicated by arrows. Asterisk marks at two peaks are from an unknown impurity phase.

representations $\Gamma_{mag} = 1\Gamma^1_1 + 1\Gamma^1_2 + 2\Gamma^2_5$ are compatible with the $P\bar{4}2_1m$ symmetry with two Fe sites at (0,0,0) and (1/2,1/2,0). The basis vectors of $2\Gamma^2_5$ reproduce all of magnetic Bragg peaks with a collinear antiferromagnetic spin structure as depicted in Fig. 7(a) and (b). The in-plane collinear AFM spin alignment indicates that the nearest neighbor spin-spin interaction is governed by the Heisenberg J_{intra} through the in-plane Fe^{2+}-O^{2-}-O^{2-}-Fe^{2+} exchange path (see Fig. 1). The ordered magnetic moment is determined to be 2.95 μ_B, which is only 74% of the full moment of Fe^{2+} spin ($S = 2$).

TABLE I. Crystallographic parameters with space group $P\bar{4}2_1m$ (SG:113) from Rietveld refinements on the diffraction data at $T = 30$ K. Lattice constants $a = b = 8.3193(8)$ Å, $c = 5.3348(5)$ Å, and $\alpha = \beta = \gamma = 90°$. $R_{wp} = 6.75\%$.

atom	*site*	*x*	*y*	*z*	B
Ba	4e	0.1648(3)	0.6648(3)	0.5090(6)	0.05(12)
Fe	2a	0	0	0	0.05(4)
Si	4e	0.3627(3)	0.8627(3)	0.9610(7)	0.12(12)
O1	2c	0	0.5	0.1371(8)	0.36(8)
O2	8f	0.3649(3)	0.8649(3)	0.2627(5)	0.17(6)
O3	4e	0.0764(3)	0.1990(2)	0.1712(4)	0.15(5)

TABLE II. Crystallographic parameters with space group $P\bar{4}2_1m$ (SG:113) from Rietveld refinements on the diffraction data at $T = 1.7$ K. Lattice constants $a = b = 8.3194(2)$ Å, $c = 5.3336(5)$ Å, and $\alpha = \beta = \gamma = 90°$. $R_{wp} = 7.14\%$.

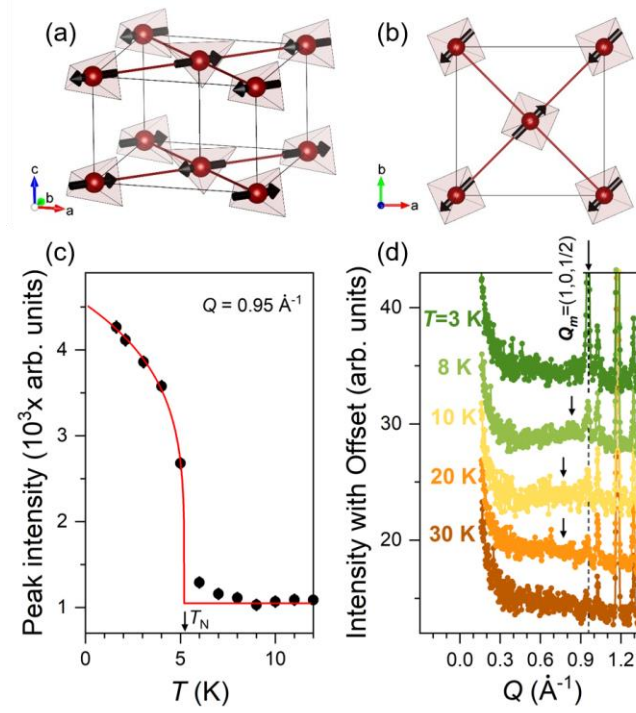| atom	*site*	*x*	*y*	*z*	B
Ba	4e	0.1644(3)	0.6644(3)	0.5098(7)	0.08(10)
Fe	2a	0	0	0	0.20(5)
Si	4e	0.3645(3)	0.8645(3)	0.9609(7)	0.11(8)
O1	2c	0	0.5	0.1383(8)	0.54(9)
O2	8f	0.3651(3)	0.8651(2)	0.2642(5)	0.07(6)
O3	4e	0.0769(3)	0.1984(2)	0.1694(5)	0.32(5)

FIG. 7. (a), (b) Magnetic structure of $Ba_2FeSi_2O_7$. The structure is a collinear spin alignment of Fe spins with $\boldsymbol{Q_m}$ = (1,0,1/2) (= 0.95 Å^{-1}). (c) Magnetic peak intensity at $Q = 0.95$ Å^{-1} as a function of temperature (black closed circles). The red solid line is a guide to eye, and $T_N = 5.2$ K is indicated by a vertical arrow. Near constant intensity above T_N reflects the structural contribution at Q. (d) Neutron powder diffraction patterns at different temperatures as indicated in the figure.

Figure 7(c) shows evolution of the magnetic peak intensity at $\boldsymbol{Q_m}$ = (1,0,1/2) ($Q = 0.95$ Å^{-1}) with temperature. Figure 7(d) presents NPD Q-scans at different temperatures from 3 K to 30 K. The sharp and intense magnetic Bragg peak, which is present at $Q = Q_m = 0.95$ Å^{-1} in the 3 K scan, mostly diminishes at 8 K. A small peak at Q_m = (1,0,1/2) ~ 0.95 Å^{-1} in 8 K data is likely due to the significant 3D short-range correlations at $T_N < T \sim T_{SO}$. Note that the small peak near $Q = 0.95$ Å^{-1} remaining at 20 K and 30 K is most likely a small impurity peak (Appendix B). Besides minimal remnant of the sharp magnetic peak, an additional broad peak feature is observable around $Q = 0.8$ Å^{-1} (marked with a black arrow) in the 8 K scan. The broad peak around Q = (1,0,0) ~ 0.75 Å^{-1} (close to 0.8 Å^{-1}) is from the 2D correlations with magnetic form factor distribution and is observed in 20 K. This feature gradually fades

15

out and shifts to low Q upon heating, and then finally disappears at 30 K, well above T_N. This Q-dependent diffusive scattering is attributed to short range spin-spin correlations, which were also observed in the magnetic specific heat $C_M(T)$ as a broad peak feature around $T_{SO} \sim$ 8 K (see Fig. 5). Presence of the diffusive scattering feature reflects strong spin fluctuations in the low dimensional quasi-2D magnetic system.

IV. DISSCUSSION

We observe multiple magnetic transitions with temperature and in-plane magnetic fields ($H\|ab\|[110]$) in the magnetization and specific heat measurements. Those transitions can be summarized with a phase diagram in an H-T space as shown in Fig. 8. The phase boundaries are defined by the peak positions determined from $d\chi/dT$, dM/dH, and C_M. At a zero field, the system is in the AFM-I phase with two types of AFM domains below T_N, and transits to the paramagnetic phase (PM) upon heating across T_N. On the other hand, as H increases across $\mu_0 H_{ab1} \sim 0.3$ T well below T_N, the AFM-I phase transits to the AFM-II phase with a single type of AFM domain. The AFM ordered spins, which lie to be nearly perpendicular to the H-direction, slightly cant toward the H-direction and result in a finite M, i.e. a composition of AFM and ferromagnetic (FM) components (field induced canted AFM). As the H-field further increases, the AFM component decreases and finally disappears. The AFM-II phase transits to the spin polarized (SP) phase across H_{ab2} with a certain gain of ΔM. $\mu_0 H_{ab2} \sim 7.4$ T determined from $M(H,T)$ at 1.8 K decreases as T increases (see Fig. 3). $H_{ab2}(T)$ nearly coincides with $T_N(H)$ from $\chi(H,T)$ (see Fig. 4) up to $T \sim 4$ K. Upon further heating, $H_{ab2}(T)$ somewhat deviates from $T_N(H)$ and finally disappears at $T > \sim 5$ K (or $\mu_0 H < \sim 4$ T), implying that the SP phase crosses over to the PM phase.

We note that $T_N = 5.2$ K at $H = 0$ increases up to 2 T and then decreases above 2 T as H increases. This non-monotonic behavior of $T_N(H)$ was also observed in other quasi-2D spin systems with a very
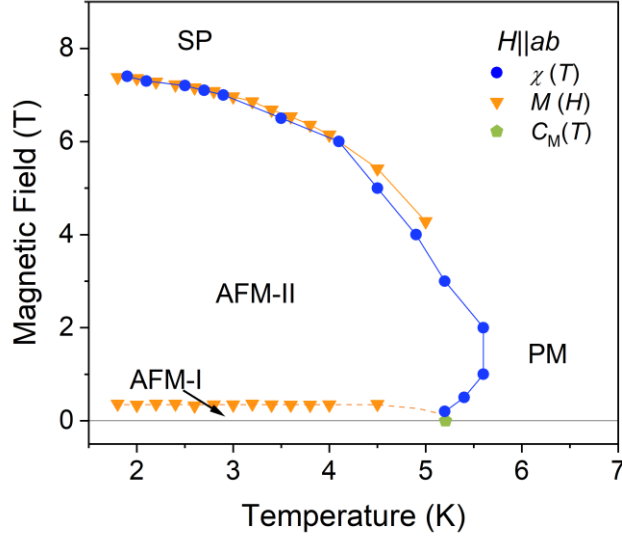
FIG. 8. Magnetic phase diagram of the $Ba_2FeSi_2O_7$ with applied magnetic field $H \| ab \| [110]$. Blue and green symbols present T_N determined from the magnetic susceptibility and specific heat measurements, respectively. Orange symbols represent critical magnetic fields (H_{ab1}, H_{ab2}) determined from the magnetization measurements. AFM-I, AFM-II, SP, and PM denote antiferromagnetic (two types of AFM domains), field induced canted antiferromagnetic, spin-polarized, and paramagnetic phases, respectively.

weak inter-layer exchange coupling (J_{inter}) [9, 10]. At a low magnetic field, the S^z spin fluctuation becomes suppressed and the spin correlation within the ab plane becomes effectively enhanced to increase T_N. At a high field, the spin canting effect prevails to reduce T_N as usual. Appearance of the non-monotonic behavior of $T_N(H)$ manifests that $Ba_2FeSi_2O_7$ is a spin system with the strong 2D character. It is also consistent with remarkable short-range spin correlation above T_N observed in specific heat and neutron diffraction results.

To quantify energy scales of the exchange interactions and single-ion anisotropy, we performed Monte Carlo simulations to calculate the magnetic properties. The calculated $\chi(T)$ and $M(H)$ are compared with the corresponding experimental ones in Fig. 2 and Fig. 3, respectively. For the simulation, we constructed a simple spin Hamiltonian only consisting of Heisenberg exchange interactions, a single-ion anisotropy, and a Zeeman term for $S = 2$ as follows;

17

$$\mathcal{H} = J_{\text{intra}} \sum_{<ij>_1} \mathbf{S}_i \cdot \mathbf{S}_j + J_{\text{inter}} \sum_{<ij>_2} \mathbf{S}_i \cdot \mathbf{S}_j + D \sum_i (S_i^z)^2 - \mu_{\text{B}} \sum_i \mathbf{S}_i \cdot \mathbf{g} \cdot \mathbf{B} \; ,$$

where $<i, j>_1$ and $<i, j>_2$ denote the in-plane and inter-plane nearest neighbors, respectively. The direction of z is parallel to the c axis (see Fig. 1(a)). Although it is not possible to uniquely determine values of the exchange parameters, we could quantify $J_{\text{intra}} = 0.15$ meV, $J_{\text{inter}} = J_{\text{intra}}/60$, and $D = 1.4$ meV, $g_{ab} = 2.6$ and $g_c = 2.3$, which fairly well reproduce T_{N}, high temperature $\chi(T)$ above 50 K (Fig. 2(a)), and the magnetic anisotropy $M(H)$ (Fig. 3(a)). $\chi(T)$ below 50 K deviates from the Curie-Weiss formula. We ascribe this deviation to thermal depopulations of the high energy spin states split by the strong single-ion anisotropy, which are not taken into in our classical Monte Carlo simulations.

Together with tetragonal compression of FeO_4 tetrahedrons along the z direction in $Ba_2FeSi_2O_7$, the spin-orbit coupling (SOC) splits the $S = 2$ state with $(2S +1)$-fold degeneracy into one singlet ground state ($S^z = 0$) and two doublet excited states ($S^z = |\pm 1>$ and $S^z = |\pm 2>$) with finite gaps of D and $3D$, respectively (see inset in Fig. 5(b)) [19-21]. Hence these low-lying ground/excited spin states are governed by thermal populations in the temperature range of $4D$ (5.6 meV $\sim$ 70 K) energy scale. The residual broad peak around 23 K in C_{M} is considered to be associated with the thermal populations of $S^z = |\pm 1>$ and $S^z = |\pm 2>$ states. The Schottky anomaly for the gap $\Delta = 3D$ with $D = 1.4$ meV from the Monte Carlo simulation (red dashed line in Fig. 5(b)) reproduces the peak position and width of the observed broad peak. This D-value agrees with the value obtained from the recent inelastic neutron scattering study [22]. The thermal populations of the excited states ($S^z = |\pm 1>$ and $S^z = |\pm 2>$) were also similarly observed in the THz absorption data of a sister compound $Sr_2FeSi_2O_7$ (denoted by β-mode absorption) [19]. It is worth to note that magnetic susceptibility along the c axis deviates from the Curie-Weiss formula below 70 K, which is consistent with the onset temperature of the Schottky anomaly peak. The deviations in χ_c and the Schottky peak evidence the presence of a single-ion anisotropy in $Ba_2FeSi_2O_7$.

V. CONCLUSION

In summary, we have studied the effects of the large single-ion anisotropy (D) on the physical properties in the new $S = 2$ quasi-2D square lattice antiferromagnet $Ba_2FeSi_2O_7$ with M, χ, C_M, and NPD measurements. The gapped spin states and their thermal populations are responsible for the remarkable 2D spin fluctuation behaviors such as Schottky anomaly and short-range magnetic ordering with strong release of the magnetic entropy gain. On the other hand, below $T_N = 5.2$ K, M and χ exhibit large easy-planar magnetic anisotropy, and the NPD data yield a significantly reduced magnetic ordered moment. As the easy-planar anisotropy gap energy D increases, the system with an integer S could favor a quantum disordered paramagnetic ground state (local $S^z = 0$) rather than the AFM one [30, 31]. We suspect that the AFM $Ba_2FeSi_2O_7$ may be near the quantum critical point of these two competing magnetic states. In this case, Higgs modes like the longitudinal magnon modes are possibly observable in the low-energy spin excitation spectra of the inelastic neutron scattering or Raman spectroscopy [22, 32-34]. The presented magnetic results and the constructed magnetic phase diagram suggest that $Ba_2FeSi_2O_7$ is an important example of the $S = 2$ quasi-2D square lattice Heisenberg antiferromagnet with a strong easy-planar magnetic anisotropy, providing a suitable playground to test intriguing physics of the low dimensional quantum magnetism.
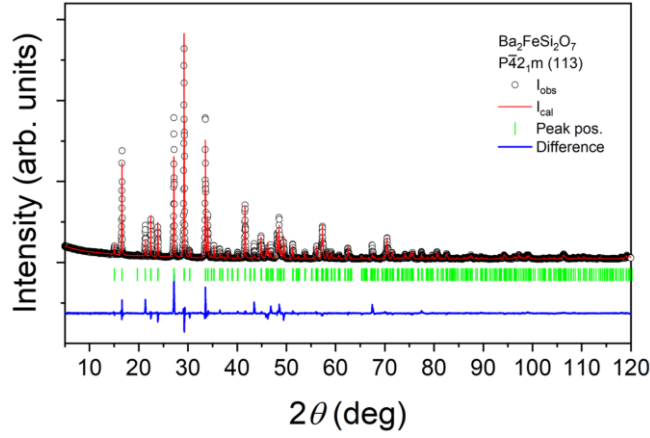
Appendix A: X-ray diffraction data for crushed single crystals

FIG. S1. X-ray diffraction (XRD) pattern from crushed single crystals of $Ba_2FeSi_2O_7$ collected at $T = 300$ K. Open circles represent experimental data and solid line in red indicates a fitted line from Rietveld refinement using FULLPROF [26]. The blue solid line indicates the difference between experimental data and the fitted line. Green tick marker indicates the location of Bragg reflections for $Ba_2FeSi_2O_7$ phase. The XRD pattern confirms the single phase $Ba_2FeSi_2O_7$ but also exhibits that there exist preferred crystallographic orientations.

TABLE SI. Crystallographic parameters with space group $P\bar{4}2_1m$ (SG:113) from Rietveld refinements on the diffraction data at $T = 300$ K. Lattice constants $a = b = 8.3261(2)$ Å, $c = 5.3402(1)$ Å, and $\alpha = \beta = \gamma = 90°$. $R_{wp} = 20.2\%$.

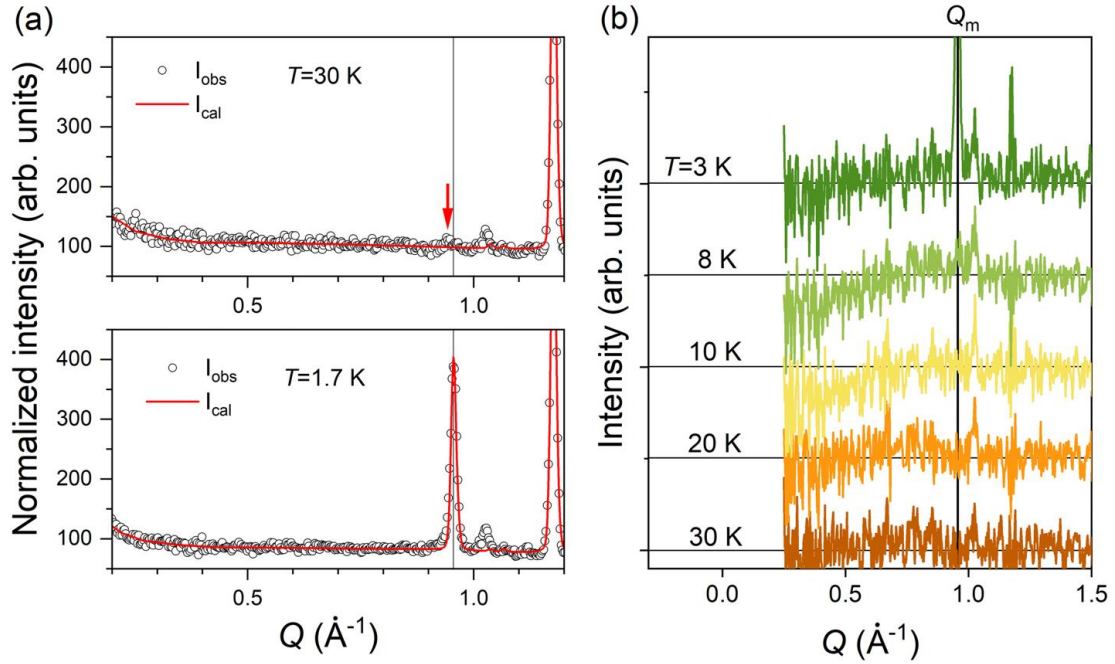| atom	site	x	y	z	B
Ba	4e	0.1693(1)	0.6693(1)	0.5098(4)	1.33(2)
Fe	2a	0	0	0	0.60(9)
Si	4e	0.3689(5)	0.8689(5)	0.9665(13)	1.17(16)
O1	2c	0	0.5	0.1182(30)	0.35(44)
O2	8f	0.3452(15)	0.8452(15)	0.2767(19)	1.85(34)
O3	4e	0.0738(12)	0.1996(11)	0.1722(11)	0.51(22)

APPENDIX B: Neutron powder diffraction data at different temperatures

FIG. S2. (a) Low Q-region of the neutron powder diffraction for $Ba_2FeSi_2O_7$ at 1.7 K and 30 K. Red arrow and solid black line indicate the remaining peak at 30 K and magnetic Bragg peak position, $Q_m = (1,0,1/2) \sim 0.95$ Å^{-1}, respectively. (b) Subtraction of the 50 K data from the low-temperature data. Horizontal solid black lines indicate the offset of each data.

Figure S2 presents the low-Q diffraction data measured at several temperatures, to show that the small peak remaining at 20 K and 30 K is most likely a small impurity peak. In Fig. S2(a), the small peak shown at 30 K (red arrow) slightly mismatches the magnetic Bragg peak at $Q_m = (1,0,1/2) \sim 0.95$ Å^{-1} (solid black line). To subtract the higher temperature data provides further clarity, Fig. S2(b) presents the subtraction of the 50 K data from the lower temperature data. In this subtracted data, the small peak is consistently absent at all temperatures. This result indicates that the peak is temperature independent across a broad temperature range, including T_N, and hence most likely arises from a small impurity phase in the sample.

REFERENCES

* All the correspondence should be addressed to jhp@postech.ac.kr.

[1] N. D. Mermin and H. Wagner, Phys. Rev. Lett. **17**, 1133 (1966).

[2] A. Orendáčová, R. Tarasenko, T. Vladimír, E. Čižmár, M. Orendáč, and A. Fehe, Crystals **9**, 6 (2019).

[3] L. Onsager, Phys. Rev. **65**, 117 (1944).

[4] A. Cuccoli, T. Roscilde, V. Tognetti, R. Vaia, and P. Verrucchi, Phys. Rev. B **67**, 104414 (2003).

[5] Y. Kohama, M. Jaime, O. E. Ayala-Valenzuela, R. D. McDonald, E. D. Mun, J. F. Corbey, and J. L. Manson, Phys. Rev. B **84**, 184402 (2011).

[6] J. M. Kosterlitz and D. J. Thouless, J. Phys. C: Solid State Phys. **6**, 1181 (1973).

[7] A. Cuccoli, T. Roscilde, R. Vaia, and P. Verrucchi, Phys. Rev. B **68**, 060402(R) (2003).

[8] N. Tsyrulin, F. Xiao, A. Schneidewind, P. Link, H. M. Rønnow, J. Gavilano, C. P. Landee, M. M. Turnbull, and M. Kenzelmann, Phys. Rev. B **81**, 134409 (2010).

[9] P. Sengupta, C. D. Batista, R. D. McDonald, S. Cox, J. Singleton, L. Huang, T. P. Papageorgiou, O. Ignatchik, T. Herrmannsdörfer, J. L. Manson, J. A. Schlueter, K. A. Funk, and J. Wosnitza, Phys. Rev. B **79**, 060409(R) (2009).

[10] E. Čižmár, S. A. Zvyagin, R. Beyer, M. Uhlarz, M. Ozerov, Y. Skourski, J. L. Manson, J. A.ˇ Schlueter, and J. Wosnitza, Phys. Rev. B **81**, 064422 (2010).

[11] P. Sengupta, A. W. Sandvik, and R. R. P. Singh, Phys. Rev. B **68**, 094423 (2003).

[12] C. Yasuda, S. Todo, K. Hukushima, F. Alet, M. Keller, M. Troyer, and H. Takayama, Phys. Rev. Lett. **94**, 217201 (2005).

[13] H. Murakawa, Y. Onose, S. Miyahara, N. Furukawa, and Y. Tokura, Phys. Rev. Lett. **105**, 137202

23

(2010).

[14] I. Kézsmárki, N. Kida, H. Murakawa, S. Bordács, Y. Onose, and Y. Tokura, Phys. Rev. Lett. **106**, 057403 (2011).

[15] S. Bordács, I. Kézsmárki, D. Szaller, N. Kida, H. Murakawa, Y. Onose, R. Shimano, T. Rõõm, U. Nagel, S. Miyahara, N. Furukawa, and Y. Tokura, Nat. Phys. **8**, 734 (2012).

[16] K. Penc, J. Romhányi, T. Rõõm, U. Nagel, A. Antal, T. Fehér, A. Jánossy, H. Engelkamp, H. Murakawa, Y. Tokura, D. Szaller, S. Bordács, and I. Kézsmárki, Phys. Rev. Lett. **108**, 257203 (2012).

[17] M. Soda, L.-J. Chang, M. Matsumoto, V. O. Garlea, B. Roessli, J. S. White, H. Kawano- Furukawa, and T. Masuda, Phys. Rev. B **97**, 214437 (2018).

[18] P. Barone, K. Yamauchi, and S. Picozzi, Phys. Rev. B **92**, 014116 (2015).

[19] T. T. Mai, C. Svoboda, M. T. Warren, T.-H. Jang, J. Brangham, Y. H. Jeong, S.-W. Cheong, and R. Valdés Aguilar, Phys. Rev. B **94**, 224416 (2016).

[20] W. Low and M. Weger, Phys. Rev. **118**, 1119 (1960).

[21] D. Dai, H. Xiang, and M.-H. Whangbo, J. Comput. Chem. **29**, 2187 (2008).

[22] S.-H. Do, H. Zhang, T. J. Williams, T. Hong, V. O. Garlea, T.-H. Jang, S.-W. Cheong, J.-H. Park, C. D. Batista, and A. D. Christianson, "Decay and renormalization of a higgs amplitude mode in a quasi-two-dimensional antiferromagnet," (2020), arXiv:2012.05445 [cond-mat.str-el].

[23] B. E. Warren, Z. Krist. **74**, 131 (1930).

[24] V. Hutanu, A. Sazonov, H. Murakawa, Y. Tokura, B. Náfrádi, and D. Chernyshov, Phys. Rev. B **84**, 212101 (2011).

[25] M. Soda, M. Matsumoto, M. Månsson, S. Ohira-Kawamura, K. Nakajima, R. Shiina, and T. Masuda, Phys. Rev. Lett. **112**, 127205 (2014).

[26] J. RodrÃguez-Carvajal, Physica B: Condensed Matter **192**, 55 (1993).

[27] A. Wills, Physica B: Condensed Matter **276-278**, 680 (2000).

[28] C. Kittel, Introduction to Solid State Physics (J. Wiley, 1995).

[29] E. Gamsjager and M. Wiessner, Monats Chem **149**, 357 (2018).

[30] Z. Zhang, K. Wierschem, I. Yap, Y. Kato, C. D. Batista, and P. Sengupta, Phys. Rev. B **87**, 174405 (2013).

[31] M. Matsumoto, M. Soda, and T. Masuda, J. Phys. Soc. Jpn. **82**, 093703 (2013).

[32] M. Matsumoto, J. Phys. Soc. Jpn. **83**, 084704 (2014).

[33] A. Jain, M. Krautloher, J. Porras, G. H. Ryu, D. P. Chen, D. L. Abernathy, J. T. Park, A. Ivanov, J. Chaloupka, G. Khaliullin, B. Keimer, and B. J. Kim, Nat. Phys. **13**, 633 (2017).

[34] S.-M. Souliou, J. Chaloupka, G. Khaliullin, G. Ryu, A. Jain, B. J. Kim, M. Le Tacon, and B. Keimer, Phys. Rev. Lett. **119**, 067201 (2017).